PHASE-FIELD MODELING OF BINARY EUTECTIC ALLOY SOLIDIFICATION WITH CONVECTION

S. Meyer, I. Otic and X. Cheng
Institute of Fusion and Reactor Technology (IFRT),
Karlsruhe Institute of Technology (KIT),
Kaiserstraße 12,
76131 Karlsruhe, Germany
stefan.meyer@kit.edu; ivan.otic@kit.edu; xu.cheng@kit.edu

ABSTRACT

In the framework of a description of melt pool heat transfer under severe accident conditions, we introduce a computational fluid dynamics approach for phase change based on the phase-field method. The approach is derived using the formalism of irreversible thermodynamics and depends on a phenomenological expression for the free energy of binary eutectic alloys. The free energy is constructed to represent the appearance of mushy layers in a volume-averaged, large scale perspective and is capable to describe sharp interfaces on sufficiently small length scales. In particular, a dynamic calculation procedure for the diffuse interface width is introduced based on free energy minimization. Numerical simulations using this approach are performed and compared with experimental and numerical results from the literature. These comparisons demonstrate that the new model improves numerical simulation results and is able to describe the dynamics of binary eutectic alloy sharp and diffuse interfaces.

KEYWORDS
melt pool heat transfer, computational fluid dynamics, phase-field, mushy layer

1. INTRODUCTION

In nuclear reactor technology, the capability of managing core melting accidents is of major importance. One possible strategy to deal with a hot corium pool accumulating in the lower head of a nuclear reactor is the in-vessel retention concept (IVR, see [1]). The idea is to keep the corium retained inside the reactor pressure vessel by providing sufficient external water cooling to prevent a vessel failure. For a successful IVR design, an accurate prediction of the melt pool heat transfer characteristics is crucial. In particular, heat transfer is strongly influenced by the flow field in the melt and its coupling to the solidification dynamics along the cooled vessel wall. As the molten core material may be described as a binary eutectic alloy ([2]), a solid-liquid mixture region can form depending on melt composition. This so-called mushy layer affects natural convection heat transfer and its properties are influenced by solute rejection and redistribution effects.
Only few computational investigations exceeding the lumped parameter methods used in severe accident system codes like MELCOR ([3]) exist in the literature. One of them is presented in [4] and [5], using the so-called effective convectivity model. Instead of solving a coupled set of Navier-Stokes and heat transport equations, the authors of this study use empirical heat transfer coefficients to determine characteristic velocities. The latter are then used in an enthalpy convection equation to transport heat from the melt pool towards the cooled walls. Modeling of phase change occurs via a latent heat term in the enthalpy equation, which depends on the local liquid fraction as a function of temperature. A newer

investigation of melt pool heat transfer is presented in [6], where a model for convection-diffusion controlled mushy region phase-change is developed based on a method by Voller ([7]). The authors solve coupled conservation equations for mass, momentum and enthalpy, but their model is two-dimensional and they neglect the transport of solute. The coupling with phase change is done like in [4], i.e. with a latent heat term depending on a purely temperature-dependent liquid fraction.
Our objective is the development of a three-dimensional computational fluid dynamics model, which couples mass-, momentum- , heat- and solute transport with an independent model for the phase change dynamics of binary eutectic alloys. A typical equilibrium phase diagram of such an alloy with components A and B is presented in Figure 1, where the composition variable c on the x-axis represents the molar fraction of component B. Due to the limited solubility of A and B in the solid state, the alloy can form two different solid phases α and β while there is only a single, homogeneously mixed liquid phase *l*. On a sufficiently small length scale, all three possible phases are separated by sharp phase boundaries. A popular tool in the literature to describe the phase change dynamics of sharp interfaces is the phase-field method ([8],[9]). Applied to the binary eutectic alloy, we introduce three phase-field functions φ_1 (liquid phase *l*), φ_2 (solid phase α) and φ_3 (solid phase β), which adopt constant values in the bulk ($\varphi_i=1$ in phase i, $\varphi_i=0$ in any other phase) and which change continuously between 0 and 1 in thin transition layers around the sharp phase boundaries (Figure 2).

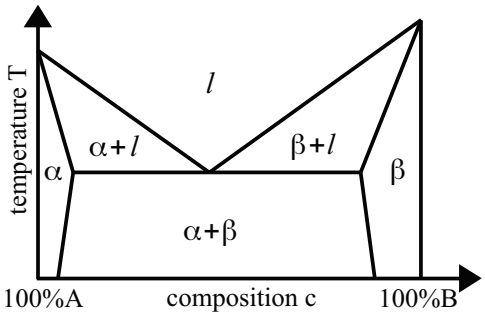

Figure 1. Binary Eutectic Alloy Phase Diagram

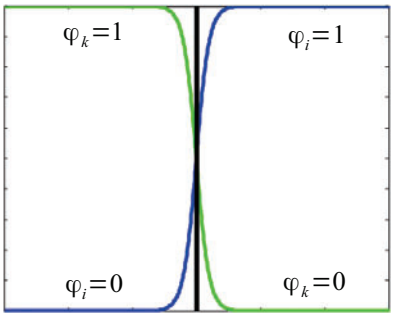

Figure 2. Phase-Field Functions around a phase boundary k-i

The regularized behaviour of the φ_i around sharp interfaces is connected to an artificial phase mixing and regarding the phase-fields as volume fractions, we must take care that they always sum up to one:

$$\varphi_1(\vec{x},t)+\varphi_2(\vec{x},t)+\varphi_3(\vec{x},t)=1 \qquad (1)$$

The triple (φ_1, φ_2, φ_3) is hence restricted to an equilateral triangle in (φ_1, φ_2, φ_3) - space, the so-called Gibbs simplex (Figure 3).

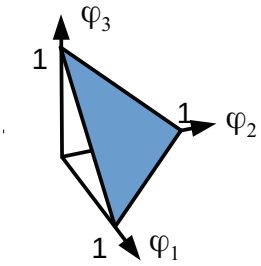

Figure 3. The Gibbs Simplex

The basic idea of the phase-field method is to avoid the tracking of sharp phase boundaries and to solve additional governing equations for the phase-field functions instead. In a thermodynamic consistent approach, a phenomenological free energy depending on the phase-field functions is constructed and the governing equations for the phase-fields as well as their coupling to other transport equations are obtained by applying thermodynamical relations and the formalism of irreversible thermodynamics.
In section 2, we will construct a free energy functional which permits an accurate reproduction of binary eutectic alloy sharp interface dynamics. After that, we make a generalization for applications on large length scales by expressing free energy in terms of the volume averages of the phase-fields in section 3. This is necessary because the sharp interface structure can be very complex and hence cannot be resolved from a large scale perspective. The volume averaging leads to the appearance of diffuse interfaces representing the aforementioned mushy layers. The generalized free energy is subsequently used in section 4 to find governing equations for the phase-change dynamics and its coupling to the velocity, the temperature and the composition field. Finally, in section 5, we present simulation results which demonstrate that our model is capable to reproduce sharp and diffuse interface dynamics of binary eutectic alloys.

2. FREE ENERGY FOR SHARP INTERFACE SOLIDIFICATION

We restrict our considerations to isothermal conditions at first and assume that the binary eutectic alloy free energy can be written as a functional according to

$$F[\varphi_1, \varphi_2, \varphi_3, c] = \int_V \{ f_s + f_b + \lambda_L \cdot T \cdot (\varphi_1 + \varphi_2 + \varphi_3 - 1) \} dV \quad . \tag{2}$$

In (2), V is the total volume of the system and the free energy density is decomposed into a surface part f_s and a bulk part f_b. The last term with the lagrangian multiplier λ_L is necessary due to the constraint (1) and as demonstrated in [10], λ_L can be determined at any instant to keep triple (φ_1, φ_2, φ_3) on the Gibbs simplex. The constant temperature factor T has been extracted from λ_L in (2) because we are mainly interested in modeling the entropic part of free energy.

2.1. Modeling of surface free energy density

In this subsection, we set $f_b \equiv 0$ and regard exclusively surface tension effects. The surface free energy density is determined by fixing the sigmoid behaviour of the phase-fields (see Figure 2) to be of a certain functional form. A popular choice in the literature is the tangens hyperbolicus profile ([10], [11]) because it allows an easy adaption of the surface free energy model to measured values of surface tension. We hence impose the condition on f_s to create the following equilibrium profiles around a sharp phase boundary between bulk phases k and i:

$$\varphi_i = \frac{1}{2} \cdot \left(1 + \tanh\left(\frac{x}{2\delta}\right)\right), \varphi_k = 1 - \varphi_i, \varphi_j = 0 \tag{3}$$

The profiles in (3) are those shown in Figure 2 and the constant length δ determines the width of the transition region between the bulk phases. For an approximation of sharp phase boundaries, δ should be as small as possible. Except for specifying the shape of equilibrium profiles, (3) also means that the mixture regions shall be purely binary, i.e. the transition layer separating a domain with phase k and a domain with phase i shall be free of the uninvolved phase j. Because thermodynamic equilibrium is characterized by a minimum of free energy, the task is to find an expression for f_s which guarantees that the free energy functional *F* in (2) is minimized by the profiles in (3). A demonstration how this can be done is given in [11], leading to the result

$$
\begin{aligned}
f_s = & -a_{12} T \delta \nabla \varphi_1 \cdot \nabla \varphi_2 - a_{13} T \delta \nabla \varphi_1 \cdot \nabla \varphi_3 - a_{23} T \delta \nabla \varphi_2 \cdot \nabla \varphi_3 \\
& + \frac{a_{12}}{\delta} T \varphi_1^2 \varphi_2^2 + \frac{a_{13}}{\delta} T \varphi_1^2 \varphi_3^2 + \frac{a_{23}}{\delta} T \varphi_2^2 \varphi_3^2 \\
& + \varphi_1 \varphi_2 \varphi_3 T \left\{ \frac{a_{12} + a_{13} - a_{23}}{\delta} \varphi_1 + \frac{a_{12} - a_{13} + a_{23}}{\delta} \varphi_2 + \frac{a_{13} - a_{12} + a_{23}}{\delta} \varphi_3 \right\}
\end{aligned}
\tag{4}
$$

with positive numbers a_{ki} , which fulfill

$$
a_{ki} + a_{kj} > a_{ij} \quad . \tag{5}
$$

The constant temperature factor has been extracted in (4) due to the same reasons mentioned before. We can regard the functional in (2) as a free energy landscape above the Gibbs simplex, which by utilizing (4) adopts minimum values of zero in the corners (bulk phases) and consists of free energy valleys along the side lines (binary interfaces). Due to the valley character of the sides, perturbations in the direction of the uninvolved phase-field (φ_j in Figure 2) correspond to a free energy increase and are damped down.

2.2. Modeling of bulk free energy density

Our modeling of the bulk free energy density is in most instances similar to the presentation in [12]. We write it as a superposition of individual phase free energy densities with appropriate interpolation functions $h_i(\varphi_1, \varphi_2, \varphi_3)$

$$
f_b = h_1 f_l(c_1, T) + h_2 f_2(c_2, T) + h_3 f_3(c_3, T) \tag{6}
$$

and interpret the composition field accordingly as a superposition of individual phase compositions c_i

$$
c = h_1 c_l + h_2 c_2 + h_3 c_3 \quad . \tag{7}
$$

It is important to note that the individual phase compositions are merely auxiliary quantities, which can be calculated from the state variables $(\varphi_1, \varphi_2, \varphi_3, c, T)$. As demonstrated in [12], the additional assumption that there is an instantaneous mass transport between locally coexisting phases leads to a condition of equal chemical potentials, which together with (7) can be used to determine the c_i .
The individual phases are assumed to represent ideal solutions of components A and B and their free energy densities are written as

$$
f_i(c_i, T) = c_i \mu_{B,i}(c_i, T) + (1 - c_i) \mu_{A,i}(c_i, T) \quad . \tag{8}
$$

The chemical potentials appearing in (8) can be adapted to describe the equilibrium phase diagram of a certain binary eutectic alloy (compare again [12]). However, because the phase change dynamics is characterized in our model by the triple (φ_1 , φ_2 , φ_3) moving in a continuous free energy landscape, we choose the interpolation functions like in [10]:

$$
h_i = \varphi_i^5 + 5 \varphi_i^4 (1 - \varphi_i) + 10 \varphi_i^3 (1 - \varphi_i)^2 + \frac{15}{4} \varphi_i^2 (1 - \varphi_i)^3 - \frac{15}{4} \varphi_i^2 (1 - \varphi_i)(\varphi_j - \varphi_k)^2 \tag{9}
$$

The reason for this complicated choice is that it guarantees a decoupling of surface effects from the bulk free energy densities. In particular, the free energy valley character of the sides of the Gibbs simplex is preserved and the equilibrium profiles (3) are uninfluenced by bulk properties.

It is now possible to calculate surface tension of a flat k-i equilibrium interface like demonstrated in [10] as the surface excess of the volume integral of the grand potential density $\omega = f - \mu c$ divided by the surface area. This allows us to relate the numbers a_{ki} to experimentally determined surface tension values according to

$$a_{ki} = 3\frac{\sigma_{ki}}{T_e} \quad . \tag{10}$$

In (10), it was assumed that the individual surface tension values were measured at the eutectic temperature T_e because this is the only temperature value at which all three possible binary interfaces can coexist in equilibrium.

3. FREE ENERGY FOR DIFFUSE INTERFACE SOLIDIFICATION

At non-eutectic compositions, there is a temperature range in which the binary eutectic alloy is neither completely liquid nor completely solid, but consists of a liquid-solid mixture (α+*l* and β+*l* in Figure 1). The detailed structure of these mixture states can be very complex. On a length scale of micrometers, it may consist of solid, tree-like dendrites, which are surrounded by interdendritic liquid. A phase-field model based on the free energy constructed in the last section for sharp interface solidification could well be used to describe the dynamics of such a structure. However, the calculation grid would have to be fine enough to resolve the continuous transitions of the phase-field functions around all the sharp interfaces of the dendritic branches. Because we are mainly interested in large scale phenomena, the required number of mesh cells would be too high for this approach to be feasible. Additionally, it is reasonable to assume that only the average properties of these mixture regions are important from a macroscopic point of view. A resolution of the detailed microstructure is hence not necessary and instead of the phase-field functions describing sharp interfaces, we regard their volume averages

$$\Phi_i(\vec{x},t) = \frac{1}{\Delta V}\int_{\Delta V} \varphi_i(\vec{x}+\vec{y},t)\,d^3y \quad . \tag{11}$$

We assume in (11) that the averaging volume ΔV is much larger than the typical length scale of the microstructure, but considerably smaller than the extent of the liquid-solid mixture region. The Φ_i are then real volume fractions of phase i because the integrand is non-zero only in phase i and the artificially introduced smooth transition layers around the actually sharp phase boundaries are negligible if the averaging volume is large enough. Consequently, we get the constraint

$$\Phi_1(\vec{x},t) + \Phi_2(\vec{x},t) + \Phi_3(\vec{x},t) = 1 \quad . \tag{12}$$

Note that $0<\Phi_i<1$ has a real physical meaning while $0<\varphi_i<1$ corresponds to an artificial phase mixture introduced by the modeling approach. Regarding a solidifying binary eutectic alloy at non-eutectic composition from a large scale perspective, the liquid volume fraction Φ_1 behaves as follows:
In regions with temperatures below the eutectic temperature, there is a completely solid state, which is in general a mixture of the two solid phases α and β. The value of the liquid volume fraction is zero there. For temperatures above the liquidus temperature, the alloy will be completely liquid corresponding to a liquid volume fraction equal to one. The layer in-between corresponds to the liquid-solid mixture discussed above and represents from a macroscopic point of view a diffuse interface between the liquid and the solid, which is often called the mushy layer. In the mushy layer, the value of the liquid volume fraction changes continuously from zero to one. In analogy to the constant length δ , which governed the width of the artificial transition layer of the φ_i around sharp phase boundaries, we introduce a non-constant length $\Delta(\vec{x},t)$ governing the width of the mushy layer.

The task is then to find a large-scale free energy

$$F[\Phi_1,\Phi_2,\Phi_3,\Delta,c]=\int_V \{f+\lambda_L\cdot T\cdot(\Phi_1+\Phi_2+\Phi_3-1)\}dV \tag{13}$$

for the binary eutectic alloy, which can be used to derive governing equations for the volume fractions Φ_i and their coupling to other transport equations of interest with the same formalism that is usually used in phase-field modeling.

It is important to note now that the phenomenology is the same as before. We have bulk phases with constant values of the Φ_i and continuous transition layers in-between. The phase diagram in Figure (1) tells us that these transition layers must be purely binary, just as we requested for the artificial transition layers of the φ_i . The only difference is that the transition layer width is a dynamical quantity now and that it does not have to be small in comparison to other lengths of interest. We can therefore make a straight-forward generalization of the free energy density constructed in the last section by replacing φ_i by Φ_i and δ by $\Delta(\vec{x},t)$:

$$\begin{aligned}
f &= f_s+f_b \\
f_s &= -a_{12}T\Delta\nabla\Phi_1\cdot\nabla\Phi_2-a_{13}T\Delta\nabla\Phi_1\cdot\nabla\Phi_3-a_{23}T\Delta\nabla\Phi_2\cdot\nabla\Phi_3 \\
&\quad+\frac{a_{12}}{\Delta}T\Phi_1^2\Phi_2^2+\frac{a_{13}}{\Delta}T\Phi_1^2\Phi_3^2+\frac{a_{23}}{\Delta}T\Phi_2^2\Phi_3^2 \\
&\quad+\Phi_1\Phi_2\Phi_3T\{\frac{a_{12}+a_{13}-a_{23}}{\Delta}\Phi_1+\frac{a_{12}-a_{13}+a_{23}}{\Delta}\Phi_2+\frac{a_{13}-a_{12}+a_{23}}{\Delta}\Phi_3\} \\
f_b &= \sum_i h_i(\Phi_1,\Phi_2,\Phi_3)f_i(c_i,T)
\end{aligned} \tag{14}$$

The a_{ki} in (14) are still given by (5).

The quantity Δ is determined as follows: Due to the slow dynamics of mushy layers, we can assume that Δ adopts at any instant its equilibrium value, i.e. the value which minimizes free energy. Because it appears only in the surface part, we find

$$\begin{aligned}
\frac{\partial f_s}{\partial\Delta} &= 0 \\
\Leftrightarrow\Delta^2 &= \frac{\sum_{i<j}\{a_{ij}\Phi_i^2\Phi_j^2\}+\Phi_1\Phi_2\Phi_3\{(a_{12}+a_{13}-a_{23})\Phi_1+(a_{12}+a_{23}-a_{13})\Phi_2+(a_{13}+a_{23}-a_{12})\Phi_3\}}{-a_{12}\nabla\Phi_1\cdot\nabla\Phi_2-a_{13}\nabla\Phi_1\cdot\nabla\Phi_3-a_{23}\nabla\Phi_2\cdot\nabla\Phi_3}
\end{aligned} \tag{15}$$

The second derivative of surface free energy density with respect to Δ is always positive such that (15) does indeed correspond to a minimum.

We investigate now the limit $\Delta V\Rightarrow 0$. By definition, we have

$$\lim_{\Delta V\Rightarrow 0}\Phi_i(\vec{x},t)=\varphi_i(\vec{x},t) \quad . \tag{16}$$

We hence must replace Φ_i by φ_i in (15). However, the value of Δ is only important in the thin transition layers separating two phases because there is no dynamics of the phase-fields in the bulk. At an equilibrium interface between phases k and i, we can put (3) into the equation for Δ and find

$$\lim_{\Delta V\Rightarrow 0}\Delta^2(\vec{x})=\frac{a_{ki}\varphi_i^2\varphi_k^2}{-a_{ki}\nabla\varphi_i\cdot\nabla\varphi_k}=\frac{\varphi_i^2(1-\varphi_i)^2}{(\nabla\varphi_i)^2}=\delta^2 \quad . \tag{17}$$

Taking (16) and (17) together, we can see that without volume averaging, the large-scale free energy functional from this section gives us back the free energy functional from section 2. Identifying the averaging volume with the volume of a computational mesh cell, we can build a theory based on (13), (14) and (15), which is capable to describe the averaged behaviour of binary eutectic alloy solidification coupled with heat, solute, mass and momentum transport from a macroscopic point of view and which converges to the correct microscopic behaviour if the computational cell size becomes sufficiently small. The latter means considerably smaller than the maximum possible width of the artificial transition layers of the φ_i , which still allows a reproduction of sharp interface dynamics.

4. GOVERNING EQUATIONS

We go to a non-isothermal scenario now, for which free energy is not the appropriate thermodynamic potential anymore. Instead, we use (13) to calculate functionals for entropy and internal energy

$$S=-\frac{dF}{dT}=\int_V\{-\frac{df}{dT}-\lambda_L(\Phi_1+\Phi_2+\Phi_3-1)\}dV \quad \text{and} \quad E=F+TS=\int_V\{f-T\frac{df}{dT}\}dV \tag{18}$$

and define an entropy per mass s_m and an internal energy per mass e_m by

$$\begin{aligned} -\frac{df}{dT}&=\sum_{i<j}a_{ij}\Delta\nabla\Phi_i\cdot\nabla\Phi_j+\rho s_m \\ f-T\frac{df}{dT}&=\rho e_m \end{aligned} \quad . \tag{19}$$

Additionally, we regard the following conservation laws for mass, momentum, internal energy and composition

$$\begin{aligned} \frac{D\rho}{Dt} &= -\rho(\nabla\cdot\vec{u}) & \rho\frac{De_m}{Dt} &= -\nabla\cdot\vec{q}_e+\boldsymbol{m}:(\nabla\vec{u}) \\ \rho\frac{D\vec{u}}{Dt} &= \nabla\cdot\boldsymbol{m}-K_0\frac{(1-\Phi_1)^2}{\Phi_1^3}+\rho\vec{g} & \frac{Dc}{Dt} &= -\nabla\cdot\vec{q}_c \end{aligned} \tag{20}$$

where the material derivative is used on the left hand sides, $\boldsymbol{m}$ is the stress tensor and velocity is damped in the mushy layer via the Darcy law with a permeability $K_0>0$.
In a first step, the internal energy per mass is taken from (19) and put into the corresponding transport equation in (20). Because $e_m=e_m(\rho,\Phi_1,\Phi_2,\Phi_3,c,T)$, we must apply the chain rule and get a transport equation for temperature with additional terms depending on the material derivatives of the phase volume fractions Φ_i and the composition field c.
After that, we apply the formalism of irreversible thermodynamics presented in [13] to find governing equations for the volume fractions Φ_i and to achieve their coupling to equations (20). Basic steps of this procedure are to regard the entropy balance of a control volume $\Omega\subset V$

$$\frac{d}{dt}\int_\Omega\{\sum_{i<j}a_{ij}\Delta\nabla\Phi_i\cdot\nabla\Phi_j+\rho s_m-\lambda_L(\Phi_1+\Phi_2+\Phi_3-1)\}d\Omega=\int_\Omega\dot{s}_p\,d\Omega-\int_{\partial\Omega}\vec{q}_s\cdot\vec{n}\,dA \tag{21}$$

and to express the entropy production rate $\dot{s}_p$ through the other quantities. The entropy per mass is then replaced by its expression in (19), $s_m=s_m(\rho,\Phi_1,\Phi_2,\Phi_3,\Delta,c,T)$, the chain rule is applied as before for the internal energy per mass and the transport equations for temperature, composition and density are

inserted. In the end, the entropy production rate is expressed as a function of $\vec{q}_s, \vec{q}_e, \vec{q}_c, \boldsymbol{m}$ and the material derivatives of the phase volume fractions Φ_i. The second law of thermodynamics requires the entropy production rate to be non-negative, which can be assured by the following constitutive laws:

$$\begin{aligned}
\vec{q}_s &= \frac{\vec{q}_e}{T} - \frac{\mu}{T}\vec{q}_c - \sum_{i<j} a_{ij}\Delta\{\nabla\Phi_i \frac{D\Phi_j}{Dt} + \nabla\Phi_j \frac{D\Phi_i}{Dt}\} \\
\vec{q}_e &= -\lambda(\Phi_1,\Phi_2,\Phi_3)\nabla T, \quad \lambda(\Phi_1,\Phi_2,\Phi_3) = \Phi_1\lambda_1 + \Phi_2\lambda_2 + \Phi_3\lambda_3 \\
\vec{q}_c &= -D\nabla c - D\sum_j (\sum_k \frac{\partial h_k}{\partial \Phi_j} c_k)\nabla\Phi_j - D_T\nabla T \\
\boldsymbol{m} &= \boldsymbol{\tau} - p\mathbf{1} + \sum_{i<j} a_{ij}\Delta\{\nabla\Phi_i\nabla\Phi_j + \nabla\Phi_j\nabla\Phi_i - (\nabla\Phi_i\cdot\nabla\Phi_j)\mathbf{1}\} \\
M^{-1}\frac{D\Phi_j}{Dt} &= \{-a_{ij}\nabla\cdot(\Delta\nabla\Phi_i) - a_{kj}\nabla\cdot(\Delta\nabla\Phi_k) + \rho(\frac{ds_m}{d\Phi_j} - \frac{1}{T}\frac{de_m}{d\Phi_j}) - \lambda_L\}
\end{aligned} \tag{22}$$

In (22), we have introduced a mixture heat conductivity $\lambda(\Phi_1,\Phi_2,\Phi_3)$, the diffusion constant D and the viscous stress tensor $\boldsymbol{\tau}$. The quantity D_T is an abbreviaton for

$$D_T = \frac{D}{(\prod_i \frac{\partial^2 f_i}{\partial c_i^2})} \sum_i h_i \frac{\partial^2 f_j}{\partial c_j^2}\frac{\partial^2 f_k}{\partial c_k^2}(\frac{\partial^2 f_i}{\partial c_i \partial T} - \frac{1}{T}\frac{\partial f_i}{\partial c_i}), \quad i \neq j \neq k \quad . \tag{23}$$

and the phase-fields' mobility is expressed as

$$M^{-1} = \frac{\Phi_2 M_{12}^{-1} + \Phi_3 M_{13}^{-1}}{\Phi_2 + \Phi_3} \quad . \tag{24}$$

The individual liquid-solid phase boundary mobilities M_{1j}^{-1} are determined in a thin-interface analysis as presented in [12] to allow a reproduction of sharp interface dynamics on small length scales.

5. SIMULATIONS

5.1 Small Length Scale

We test the capability of our model to describe sharp phase boundaries on small length scales, i.e. in the limit $\Delta V \Rightarrow 0$. Therefore, we regard a triple junction between two solid α grains and the liquid phase of the binary eutectic alloy $CBr_4 - C_2Cl_6$ in a constant temperature gradient G (Figure 4).

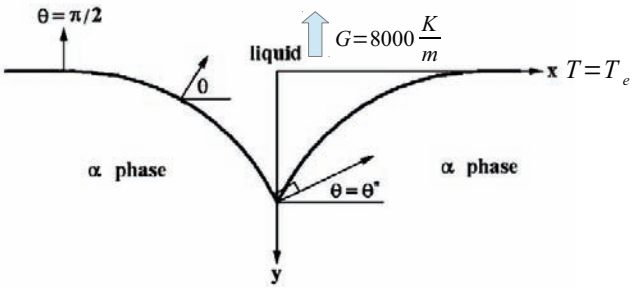

Figure 4. Simulation setup taken from [12]

The resulting equilibrium shape corresponds to a balance between Gibbs-Thomson curvature undercooling and thermal undercooling generated by the temperature gradient. This setup has been chosen in [12] for testing their model because a sharp-interface solution for comparison can be easily obtained by the following relations:

$$\begin{aligned} x &= \frac{v_m m_{12}}{R T_e (k_{12}-1) G} \int_{\theta^*}^{\theta} \frac{\sin\theta}{y} \sigma_{12} d\theta \\ y &= \frac{2 v_m m_{12}}{R T_e (k_{12}-1) G} \sigma_{12} (1-\sin\theta) \\ 0 &= \sigma_{22} - 2\sigma_{12}\cos\theta^* \end{aligned} \tag{25}$$

In (25), the molar volume v_m and the ideal gas constant R are used together with the liquid-α equilibrium partition coefficient k_{12}, the slope of the corresponding liquidus line m_{12}, the eutectic temperature T_e, liquid-α surface tension σ_{12} and surface tension between the two solid grains σ_{22}. In our simulations, we formally distinguish the two α grains by identifying one of them with the phase-field φ_2 and the other one with the phase-field φ_3. However, both phase-fields φ_2 and φ_3 are assigned with the same material properties corresponding to solid phase α. The calculations are performed with a small and constant value of $\delta = 0.12\,\mu m$ and a grid spacing of $\Delta x = 0.2\,\mu m$. Due to the small length scale, convectional effects can be neglected and we can limit ourselves to a solution of the phase-field and solute transport equations. We performed several simulations for different values of σ_{22} ranging from $\sigma_{22}=\sigma_{12}$ until $\sigma_{22}=1.95\sigma_{12}$, which is close to the limit of condition (5). The simulation results are compared with the sharp interface solution from (25) in Figure 5 and show a good agreement.

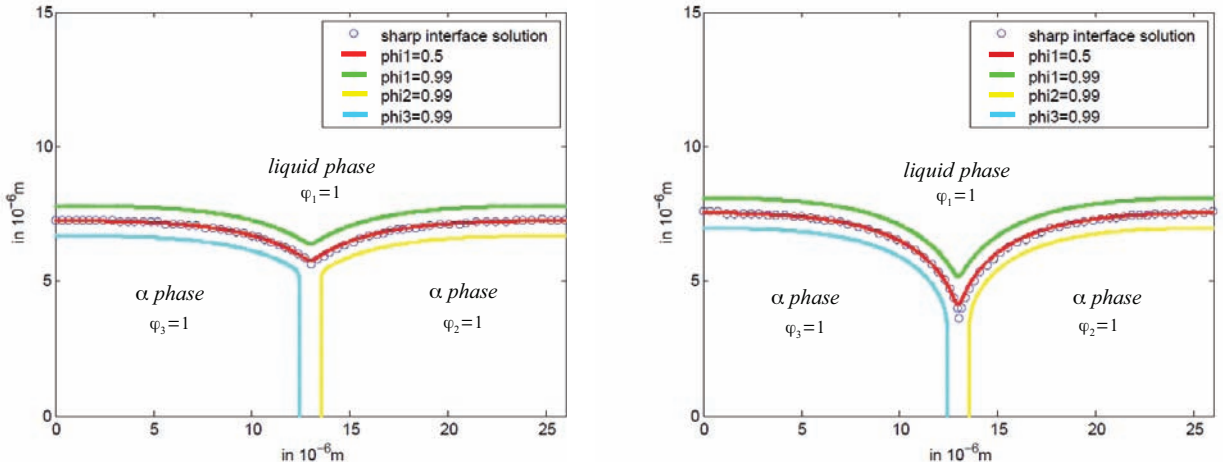

Figure 5. Equilibrium boundary shapes for $\sigma_{22}=\sigma_{12}$ (left) and $\sigma_{22}=1.95\sigma_{12}$ (right)

5.2 Large Length Scale

For a validation of the model on large length scale, we simulate an experiment performed by Christenson et al. ([14]). The authors investigated thermosolutal convection of aqueous ammonium chloride solution (NH_4Cl-H_2O) with a eutectic point ($c_e=0.803$, $T_e=-15.4\,°C$) in a cubic box of dimensions 36mm x 144mm x 200mm. One of the two vertical walls with a height of 144mm and a width of 200mm

was cooled down to a temperature of -30°C, the opposite wall was heated to +40°C. The Rayleigh number corresponding to this temperature difference and their distance of 36mm is about 10^6. We can hence conclude that turbulent effects are negligible and that the flow can be regarded as being essentially two-dimensional. The experiment was performed with an initial composition of $c = 0.7$ and a mushy layer started to grow from the cooled wall, separating the composite solid (α+β) from the liquid. During solidification, the lighter water was rejected in the mushy layer and rose upwards due to buoyancy effects, leading to a decrease of the liquidus temperature. Additionally, heat was transported upwards by ascending fluid along the heated wall. Both of these effects reduced solidification in the upper part of the box.

In our simulations, we assumed the flow to be two-dimensional and incompressible, the grid spacing was 0.5mm and we used the material properties of aqueous ammonium chloride presented in [15]. The Darcy constant K_0 was regarded as a fitting parameter and the best results were obtained for a value of $2 \cdot 10^{11}$. Figure 6 presents a comparison between the experimental results, our simulation results and the results of the simulations performed in [14]. The color map represents the simulated liquid volume fraction Φ_1 with the red color indicating completely liquid regions and the blue color referring to the pure solid. Because the border of the mushy layer towards the liquid showed a highly irregular structure in the experiments due to dendrite growth, the black dashed lines indicate like in [14] the experimentally determined average extent of the mushy layer. Our simulations show a good agreement with the experimental results and even the above mentioned irregularities are reproduced. Additionally, the authors of [14] made their own simulations (red solid lines) and achieved a worse accordance with the measurements. As they also solve a coupled system of Navier-Stokes-, heat and solute transport equations, their model is not too different from ours. However, they do not use independent governing equations for the phase change, but simply determine the phase state from the local temperature.

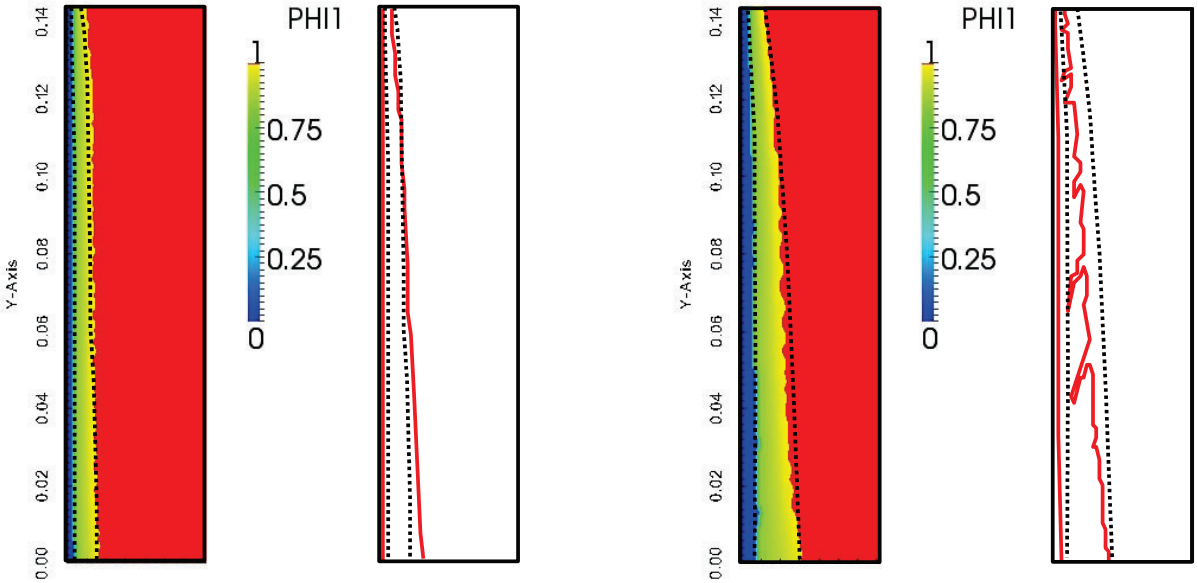

Figure 6. Comparison between experimentally determined extent of the mushy layer (dashed lines), our simulations (color map) and the simulations performed in [14] (red solid lines) at t=3min (left) and t=11min (right)

Additionally, Figure 7 shows the velocity field, the composition field and the temperature field obtained from our simulations at t=11min. The velocity field displays a counterclockwise circulation cell driven by

thermal buoyancy along the heated wall on the right. The composition field shows a uniform composition in the liquid in accordance with its initial value $c = 0.7$. However, there are inhomogeneities in the mushy layer because water is rejected from the solid and accumulates in the upper part due to solutal buoyancy. This influences the local liquidus temperature and therefore the solidification dynamics. The temperature field illustrates the effect of thermal buoyancy as there is an accumulation of heat in the upper part of the box.

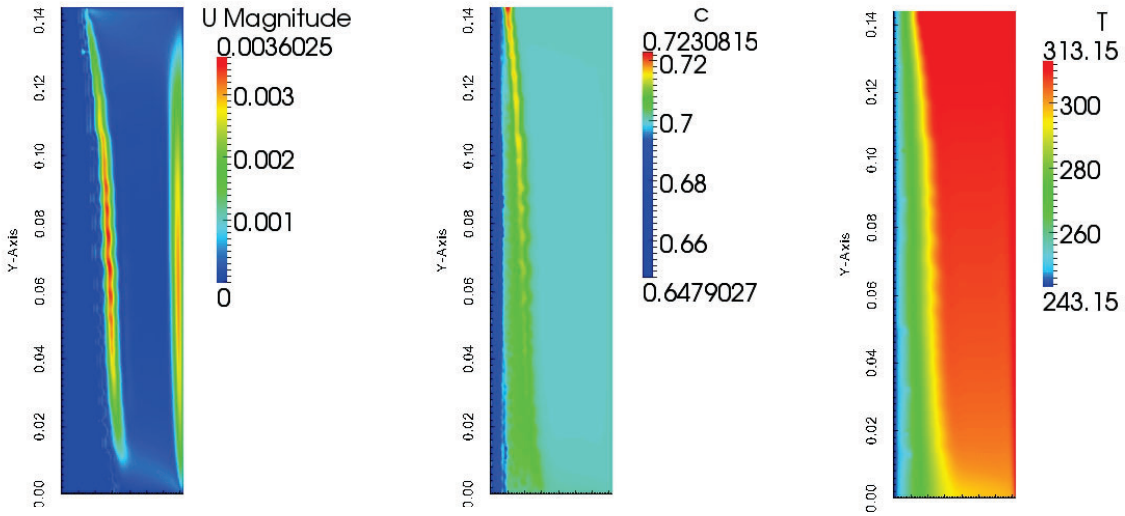

Figure 7. Velocity field, composition field and temperature field at t=11min

6. CONCLUSIONS

In this work, a phase change model for binary eutectic alloy solidification was coupled with the Navier-Stokes equations and transport equations for heat and solute in a thermodynamic consistent manner. The phase change model depends on a phenomenological free energy functional and is based on the phase-field method. It has the capability to describe the dynamics of sharp phase boundaries on small length scales. A generalization to large length scales is achieved by expressing free energy through the volume-averaged phase-fields and by a dynamic calculation procedure for the diffuse interface width on the basis of free energy minimization. Applied on large length scales, the model represents the solidification dynamics of binary eutectic alloys with mushy layers. Comparisons with sharp interface solutions and experimental results for mushy layer solidification show a good agreement. However, the model is in its current state not ready for investigations of severe accidents in nuclear reactors. Due to the high Rayleigh numbers of the core melt, turbulence modeling must be included into the model for a proper application in this field.

ACKNOWLEDGMENTS

The authors would like to acknowledge financial support from German Federal Ministry for Economic Affairs and Energy.

REFERENCES

1. C.G. Theofanous et al. , "In-vessel coolability and retention of a core melt", *Nuclear Engineering and Design* **169**, pp. 1-48 (1997).
2. B.R. Sehgal, V.A. Bui, T.N. Dinh, J.A. Green, G. Kolb, "SIMECO Experiments on In-Vessel Melt Pool Formation and Heat Transfer with and without a Metallic Layer", http://www.iaea.org/inis/collection/NCLCollectionStore/_Public/44/026/44026298.pdf
3. R. O. Gauntt et al., "MELCOR Computer Code Manual", Package Reference Manuals Version 1.8.5, NUREG/CR-6119, Vol. 2, Rev. 2
4. C.-T. Tran, T.-N. Dinh, "The effective convectivity model for simulation of melt pool heat transfer in a light water reactor pressure vessel lower head. Part 1: Physical processes, modeling and model implementation", *Progress in Nuclear Energy* **51 ,** pp. 849-859 (2009)
5. C.-T. Tran, T.-N. Dinh, "The effective convectivity model for simulation of melt pool heat transfer in a light water reactor pressure vessel lower head. Part 2: Model assessment and application", *Progress in Nuclear Energy* **51 ,** pp. 860-871 (2009)
6. Y. P. Zhang et al., "Numerical study on the heat transfer characteristics of LIVE-L4 melt pool with a partial solidification process", *Progress in Nuclear Energy* **74,** pp. 213-221 (2014)
7. V. R. Voller and C. Prakash, "A fixed grid numerical modelling methodology for convection-diffusion mushy region phase-change problems", *Int. J. Heat Mass Transfer* **30,** pp. 1709-1719 (1987)
8. W. J. Boettinger, J. A. Warren, C. Beckermann, A. Karma, "Phase-Field Simulation of Solidification", *Annu. Rev. Mater. Res.* **32,** pp. 163-194 (2002)
9. Ingo Steinbach, "Phase-Field Models in Materials Science", *Modelling Simul. Mater. Sci. Eng.* **17** (2009)
10. R. Folch, M. Plapp, "Quantitative Phase-Field Modeling of Two-Phase Growth", *Physical Review E* **72** (2005)
11. R. Haas, "Modeling and Analysis for General Non-Isothermal Convective Phase-Field Systems", PhD-Thesis (2007), http://epub.uni-regensburg.de/10538/1/diss_robert_haas.pdf
12. S. G. Kim, W. T. Kim, T. Suzuki, M. Ode, "Phase-Field Modeling of Eutectic Solidification", *Journal of Crystal Growth* **261,** pp. 135-158 (2004)
13. D. M. Anderson, G. B. McFadden, A. A. Wheeler, "A Phase-Field Model of Solidification With Convection", *Physica D* **135**, pp. 175-194 (2000)
14. M. S. Christenson, W. D. Bennon and F. P. Incropera, "Solidification of an aqueous ammonium chloride solution in a rectangular cavity-II. Comparison of predicted and measured results", *Int. J. Heat Mass Transfer* **32,** pp. 69-79 (1989)
15. M. A. Rady, S. A. Nada, "Solidification of hypereutectic and hypoeutectic binary alloys with buoyancy and surface tension driven natural convection", *Heat and Mass Transfer* **34,** pp. 337-347 (1998)